

An experimental study of residual stress and direction-dependence of fatigue crack growth behaviour in as-built and stress-relieved selective-laser-melted Ti6Al4V

Syed, A., Ahmad, B., Guo, H., Machry, T., Eatock, D., Meyer, J., Fitzpatrick, M. & Zhang, X.

Author post-print (accepted) deposited by Coventry University's Repository

Original citation & hyperlink:

Syed, A, Ahmad, B, Guo, H, Machry, T, Eatock, D, Meyer, J, Fitzpatrick, M & Zhang, X 2019, 'An experimental study of residual stress and direction-dependence of fatigue crack growth behaviour in as-built and stress-relieved selective-laser-melted Ti6Al4V', *Materials Science and Engineering: A*, vol. 775, pp. 246-257.
<https://dx.doi.org/10.1016/j.msea.2019.04.023>

DOI 10.1016/j.msea.2019.04.023

ISSN 0921-5093

Publisher: Elsevier

NOTICE: this is the author's version of a work that was accepted for publication in *Materials Science and Engineering: A*. Changes resulting from the publishing process, such as peer review, editing, corrections, structural formatting, and other quality control mechanisms may not be reflected in this document. Changes may have been made to this work since it was submitted for publication. A definitive version was subsequently published in *Materials Science and Engineering: A*, [775], (2019) DOI: 10.1016/j.msea.2019.04.023

© 2019, Elsevier. Licensed under the Creative Commons Attribution-NonCommercial-NoDerivatives 4.0 International
<http://creativecommons.org/licenses/by-nc-nd/4.0/>

Copyright © and Moral Rights are retained by the author(s) and/ or other copyright owners. A copy can be downloaded for personal non-commercial research or study, without prior permission or charge. This item cannot be reproduced or quoted extensively from without first obtaining permission in writing from the copyright holder(s). The content must not be changed in any way or sold commercially in any format or medium without the formal permission of the copyright holders.

This document is the author's post-print version, incorporating any revisions agreed during the peer-review process. Some differences between the published version and this version

may remain and you are advised to consult the published version if you wish to cite from it.

An experimental study of residual stress and direction-dependence of fatigue crack growth behaviour in as-built and stress-relieved selective-laser-melted Ti6Al4V

Abdul Khadar Syed^{1*}, Bilal Ahmad¹, Hua Guo², Thays Machry³, David Eatock³,
Jonathan Meyer⁴, Michael E. Fitzpatrick¹, Xiang Zhang¹

¹Faculty of Engineering, Environment and Computing, Coventry University, Priory
Street, Coventry CV1 5FB, UK

²The Institute for Advanced Manufacturing and Engineering, Coventry University,
Beresford Avenue, Coventry CV6 5LZ, UK

³Airbus Group Innovation, Bristol, U.K

⁴APWORKS GmbH, Willy-Messerschmitt-Straße 1, 82024 Taufkirchen, Germany

*Corresponding author; Email address: abdul.syed@coventry.ac.uk (AK Syed),
bilal.ahmed@coventry.ac.uk (B Ahmad); hua.guo@coventry.ac.uk (H Guo);
thays.machry@airbus.com (T Machry); david.eatock@airbus.com (D Eatock);
jmeyer@apworks.de (J Meyer); michael.fitzpatrick@coventry.ac.uk (ME Fitzpatrick);
xiang.zhang@coventry.ac.uk (X Zhang)

Abstract

Selective-laser-melting (SLM) is a powder-bed fusion additive-manufacturing process that has potential to deliver three-dimensional complex parts with mechanical properties comparable or superior to parts produced via traditional manufacturing using cast and wrought alloys. Concerns for metallic parts built via SLM are the process-induced residual stresses, and anisotropic mechanical properties. This paper investigates the effect of residual stresses on the fatigue crack growth rate of SLM Ti6Al4V in as-built and stress-relieved conditions. Neutron diffraction and the contour method are employed to measure residual stresses in compact-tension samples. Neutron diffraction results are in good agreement with the contour method. It was found that tensile stresses are present at the notch root and the free edge areas, and compressive stress is seen in the middle of the sample. The tensile stresses in the as-built condition resulted in a higher fatigue crack growth rate. After stress relieving by heat treatment, the tensile residual stress diminished by around 90%, resulting in decreased crack growth rate. The build direction was seen to

affect the crack growth rate, although the trend was different between the as-built and stress-relieved conditions.

Keywords: Additive manufacturing, Contour method, Fatigue crack propagation, Residual stress, Selective laser melting, Titanium alloys

1. Introduction

Titanium alloy Ti6Al4V is widely used in the aerospace industry to produce parts which require high strength, low density, excellent corrosion resistance, and unique combination of fatigue crack growth resistance and ductility [1,2]. Also, its biological and chemical compatibility have extended its application to the biomedical sector [3]. Selective Laser Melting (SLM) is an additive manufacturing process that can deliver complex three-dimensional geometries produced in a layer-by-layer fashion directly from powder bed using a high-energy laser beam. Several metallic materials such as aluminium [4,5], nickel alloys [6–8], stainless steel [9], and titanium alloys [10–15] have been built using SLM. The highly localised laser beam with very short interaction times produces complex residual stresses during the melting and cooling cycles of the deposited layer [16–19]. During the melting, owing to the rapid heating of the powder particles, a large thermal gradient will develop between the top and the underlying layers. This phenomenon is known as the thermal gradient mechanism (TGM) [17]. Since the underlying materials hinder the expansion of the heated top layer, elastic compressive stresses will develop in the material. When the material's yield strength is reached, the top layer will be plastically compressed. This phenomenon can occur without the necessity of complete re-melting of the top layer [17]. Residual stresses can lead to deformation and cracks in the parts and sometimes delamination from the base plate [20].

In recent years, much research has focused on the influence of process parameters on residual stresses [18,19,21,22] microstructure [23–28], and mechanical properties [21,24,26,29,30] of parts produced by SLM processing. Directional solidification associated with SLM process results in columnar retained β grains aligned along the build direction. Within retained β grains, a very fine needle-like acicular martensite (α') phase is present as a result of a diffusionless, shear-type transformation process [10,27]. SLM Ti6Al4V is also associated with strong crystallographic texture and anisotropy in mechanical properties [26,31]. Yield strength and the ultimate tensile strength of as-built Ti6Al4V are 16% and 33% higher than the wrought material due to the presence of α'

martensite. However, the ductility is 48% lower for SLM Ti6Al4V when compared to the wrought material [31]. Residual stresses in SLM parts can be controlled by varying scanning strategy by lowering thermal gradients between the scanning tracks. Shorter deposition by carefully rotating the scan pattern between the successive layers will create a more homogenous solidification process thereby lowering the temperature gradient and process-induced residual stresses [21,32,33]. Residual stresses can also be lowered efficiently by subjecting the part to a post-fabrication heat treatment process, often known as a stress-relieving heat treatment [34].

Among the major additive manufacturing technologies, the magnitude of process-induced residual stress is high in SLM process [16–19]. Therefore, several studies have been performed to understand the residual stress development and their influence on mechanical properties [17,18,35]. Tensile residual stresses along the deposition direction can significantly reduce the fatigue strength by decreasing the crack initiation period and increasing the crack growth rate [15,36,37]. In recent studies [13,18], as-built Ti6Al4V with a crack perpendicular to the build direction showed higher crack growth rate due to the presence of residual stresses along the loading direction. Mercelis *et al.* [17] proposed a simplified theoretical model to predict the residual stresses in SLM materials. The residual stress profile mainly consists of three zones: large tensile stresses at the top and bottom of the part, and an intermediate compressive zone in the middle. The magnitude of the residual stress depends on the material properties, substrate thickness, build height and the laser scanning strategy. An increase in the number of layers will increase the residual stress [17]. Vrancken *et al.* [18] used the contour method to determine the residual stresses in as-built samples and found a similar three zones as in [17]. Rangaswamy *et al.* [35] used neutron diffraction and the contour method to investigate the effect of various deposition strategies on residual stresses in rectangular blocks of 316 stainless steel and Inconel 718 deposited using laser engineered net shaping (LENS) process. The result showed that the residual stresses mainly aligned along the build direction with tensile stress along the outer surfaces and compression in the middle of the sample [35].

So far, numerous studies have focused on the process, microstructure, defects and static behaviour of SLM Ti6Al4V, but the only study on residual stress and its influence on fatigue performance is limited and semi-quantitative [18]. Moreover, modelling of

residual stress in SLM is difficult due to the complex thermal gradients and the localized phenomena of melting and solidification involved during the process. Tensile residual stress in SLM will increase the fatigue crack growth rate, thereby degrading the ability of the component to serve in its intended application and limiting the industrial adoption of Ti6Al4V components produced via the SLM process. Furthermore, it is important to take account of residual stress in the initial design and stress analysis stages. Hence, it is necessary to understand the relation between the processing and residual stress developed in the parts, and the effect of post-process heat treatment. Therefore, this paper is focused on systematic analysis of residual stresses and their effect on fatigue crack growth rate of SLM Ti6Al4V samples in the as-built and stress-relieved conditions.

2. Materials and methods

Samples were produced by using Grade 5 Ti6Al4V powder on an SLM machine EOS M270 using standard optimised process parameters for Ti6Al4V supplied by EOS. The chemical composition of the powder is O=0.19%, N=0.045%, H=0.006%, C=0.015%, Al=6.4%, V=4.4%, Fe=0.13%, Y<0.01% and balance Ti. The powder is produced by gas atomisation. Eighteen rectangular blocks of $42 \times 42 \times 8 \text{ mm}^3$ were built in two orientations as shown in Fig 1a. The samples are termed vertical or horizontal builds, depending on the sample orientation relative to the base plate. Relative to the XYZ axis system, the samples are termed, for example, XZ to indicate the plane of the largest face of the C(T) samples, with the second letter indicating the direction of crack growth. All the blocks were deposited with a layer thickness of $30\mu\text{m}$. After the deposition, the blocks are separated from the base plate. Nine blocks (three in each orientation, XY, ZX and XZ) are used to manufacture the as-built samples and the remaining nine blocks (three in each direction orientation, XY, ZX and XZ) are stress-relieved at 680°C for 3h under inert gas. All test samples are in compact tension (C(T)) geometry, that were machined and notched.

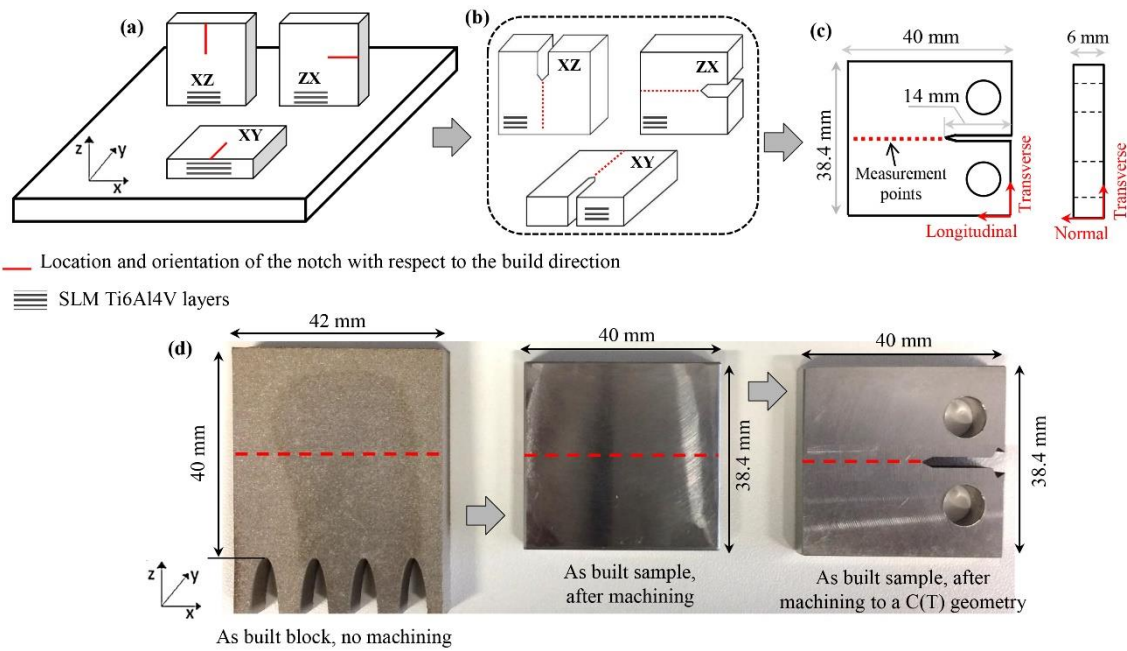


Fig. 1: Schematics of (a) rectangular blocks deposited in different heights (z-axis) and width (y-axis) on a base plate; block size: $42 \times 40 \times 8 \text{ mm}^3$ (b) C(T) samples machined from the rectangular blocks (removing 1 mm from the surface, and adding a notch). (c) Geometry and dimensions of the C(T) sample used for residual stress measurements using neutron diffraction and fatigue crack growth testing. Dotted line indicates the residual stress measurement points using neutron diffraction and crack growth path. The dimensions are not to scale. (d) Actual vertical built (ZX) sample showing rectangular block and C(T) sample machining from the built block. Dotted lines indicate the contour cut path.

As-built and stress-relieved blocks were then machined to $40 \times 38.4 \times 6 \text{ mm}^3$ to manufacture C(T) samples, Fig. 1b. C(T) samples were designed according to ASTM standard E647 with three different notch positions with respect to the build direction. The notch was produced using electro-discharge machining. The longest dimension (40 mm) of the sample is always parallel to the notch. A schematic of the C(T) used for residual stresses and fatigue crack growth measurements is shown in Fig. 1c. The longest dimension (40 mm) is defined as the longitudinal direction, the direction across the width (38.4 mm) is referred to as the transverse direction, and the through-thickness dimension (6 mm) is referred to as the normal direction.

2.1. Microstructural analysis

Microstructure characterisation was performed using a Zeiss Gemini 500VP scanning electron microscope (SEM), and with optical microscopy. For this, samples were prepared with standard metallographic procedures, including mounting, grinding with SiC papers up to grit size of 2500, and polishing using diamond suspension down to 1µm followed by final polishing with colloidal silica of 0.02µm particle size. For microstructural analysis, samples were etched with Kroll's reagent (96 ml H₂O, 2 ml HF, and 6 ml HNO₃) for 45 seconds.

2.2. Residual stress analysis

Residual stress was determined experimentally using neutron diffraction and the contour method. The following section provides a detailed description of the residual stress experimentation.

2.2.1 Neutron diffraction

Neutron diffraction measurements were performed only on the samples in the as-machined condition. Neutron diffraction is a well-established non-destructive technique with large penetration depths to provides strains within bulk materials and engineering structures. The principle of neutron diffraction is based on Bragg's law which is used to determine the change in lattice parameter owing to tensile or compressive stress within the material. Residual stress measurements were performed in three orthogonal directions using the ENGIN-X time-of-flight diffractometer at the UK's ISIS pulsed neutron source. ENGIN-X consists of two detectors placed at ± 90° to the incident beam that allows measurement of strain in two directions simultaneously [38]. The diffracted beam from the sample contains multiple reflections that are then collected by the detectors. The data collected were analysed by ENGIN-X Script Based Analysis (EX-SBA) software that uses Pawley or Rietveld refinement to determine the lattice spacing (a) in the measured direction, which can be used to determine strains by equation 1.

$$\varepsilon(x, y, z) = \frac{a(x,y,z) - a_0}{a_0} \quad (1)$$

Where $\varepsilon_{(x,y,z)}$ is the strain in the respective direction, $a_{(x,y,z)}$ is the measured lattice spacing and a_0 is the stress-free reference lattice parameter. The stress can be computed by using the tri-axial form of the Hooke's law.

$$\sigma_x = E \frac{(1 - \nu)\varepsilon_x + \nu(\varepsilon_y + \varepsilon_z)}{(1 + \nu)(1 - 2\nu)} \quad (2)$$

Where E is Young's modulus of Ti6Al4V, ν is the Poisson's ratio. Six points were measured in each sample with a gauge volume of $2 \times 2 \times 8 \text{ mm}^3$ for the longitudinal measurements and $2 \times 2 \times 4 \text{ mm}^3$ for the transverse and normal measurements. The longest dimension of the gauge volume was always aligned along the transverse direction (Fig. 1c) to increase the counting statistics. The first measurement point is at 3 mm from the notch root followed by a 4 mm measurement density along the longitudinal direction. Stress-free (a_0) measurements were performed on $6 \times 6 \times 6 \text{ mm}^3$ samples exacted from the as-built and virtually stress-relieved samples close to the edge. A gauge volume of $3 \times 3 \times 3 \text{ mm}^3$ was used for all the a_0 measurements.

2.2.2 Contour measurements

The contour method is a residual stress determination technique based on the stress relaxation in a part when it is cut into two halves. The measured stress component is always normal to the cut surface [39]. Samples were cut using a 0.25-mm-diameter brass wire using low power cutting parameters on a wire electro-discharge machine. The contour cut was performed along the transverse direction (refer to the dotted lines in Fig. 1d). The cut progressed smoothly without wire breakage or any significant variation in the cutting speed. The surface displacement profile of the cut surfaces of the samples was measured with a Zeiss Contura g2 coordinate measuring machine. A 3-mm-diameter touch probe was used. The distance from the perimeter and between the individual measurement points in both directions on the sample surface was set as 0.1 mm. The measured displacement data from both cut surfaces of each sample was post-processed for data aligning, cleaning, flattening and smoothing using Matlab analysis routines. Contour measurements were performed on samples that were as-built with no machining; machined to a rectangular block; machined to the C(T) geometry; and stress-relieved with C(T) geometry (refer Fig. 1d). The data smoothing was performed with a cubic spline knot spacing of 3.5 mm for as-built and machined samples, and 8 mm for the stress-relieved sample, for both X and Y directions. A linear-elastic finite-element (FE) model of one cut half of the sample was constructed using Abaqus software. An 8-node brick element (C3D8R) was selected with a uniform mesh size on the cut surface of 0.2 mm.

2.3. Fatigue crack growth testing

For each crack orientation, three samples of the as-built and stress-relieved conditions were tested for the fatigue crack growth rate at room temperature using a 10 kN Instron servo-hydraulic test machine. Tests were performed at constant amplitude load according to the ASTM standard E647. Samples were subjected to a maximum load of 3 kN with a load ratio R of 0.1 at 10 Hz frequency. Crack length measurement was performed with a travelling microscope with $7\times$ objective magnification and with an accuracy of ± 0.01 mm. The anticipated crack path was polished. Fatigue crack growth rate was deduced from the crack length vs fatigue cycle curve using the 7-point polynomial method.

3. Results and discussion

3.1. Characterisation of as-received powder

The Ti6Al4V powder used in this study was produced by gas atomisation. Fig. 2a and 2b show the secondary electron SEM images of powder in the as-received condition. The powder particles are spherical but occasionally irregular shaped particles were also observed. The particle size distribution is in the range of: 35% $<45\ \mu\text{m}$; 61% $45\text{-}105\ \mu\text{m}$; and 4% $>105\ \mu\text{m}$. Larger powder particles were found having some satellite particles ($<10\ \mu\text{m}$) resulting from the powder manufacturing process. Fig. 1a also shows a large fraction of powder particles smaller than $45\ \mu\text{m}$ that correspond to the satellite powder particles. Furthermore, hollow powder particles (Fig. 2b) are occasionally observed due to gas being entrapped in these particles during the gas atomisation process.

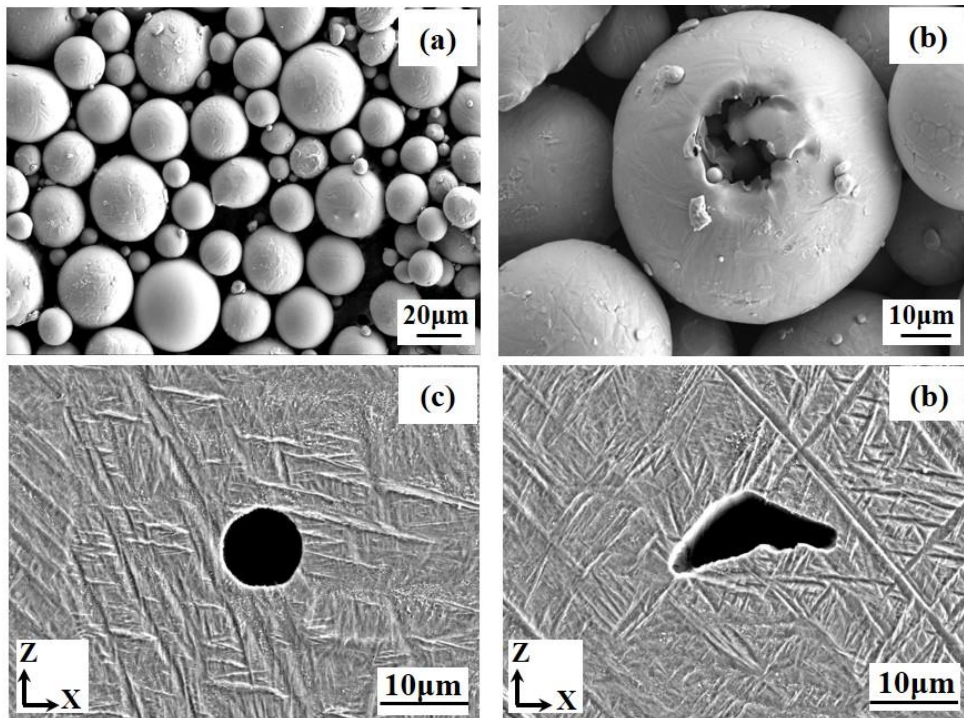


Fig. 2: SEM images showing (a) spherical powder particles with homogeneous distribution. Fine satellite particles adhering to large powder particles can be observed. (b) Occasionally, a pore in powder particles is observed which resulted from gas entrapment during the gas atomisation process. (c) and (d) gas pore and lack-of-fusion defect found in as-built sample

3.2. Microstructure in as-built and stress-relieved conditions

During the microstructural analysis, it was observed that both spherical gas pores and lack-of-fusion pores are present in as-built and stress-relieved samples (see Fig. 2c and 2d). Gas pores and lack-of-fusion pores are typically formed in powder-bed additive manufacturing processes and have been reported previously [26,40]. The observed gas pores are near-spherical in shape, with size ranging from 5-34µm. The formation of spherical pores might be attributed to vaporisation of low melting point constituents within the alloy, and entrapped argon gas during the gas atomisation powder fabrication process [41]. This is true in this research as occasionally hollow powder particles are observed (Fig. 2b).

Fig. 3 shows optical micrographs of the as-built and stress-relieved conditions. Both microstructures show columnar prior-β grains aligned along the build direction (Z-axis) as a direct consequence of directional solidification and large thermal gradients along the build direction. These columnar grains grow across many deposited layers. Such

a columnar β microstructure is typically observed in most additive manufacturing processes as reported by several authors [42–45]. The average width of the prior- β grains in the as-built condition is $90\pm 20\mu\text{m}$.

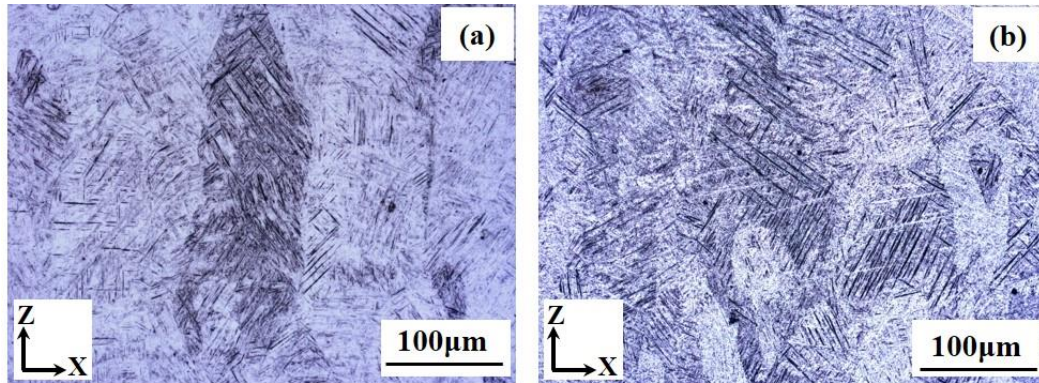


Fig. 3: Optical micrographs showing microstructure along the build direction showing epitaxial growth of columnar prior- β grains in (a) as-built (b) stress-relieved condition (bright phase indicates α and dark phase indicates β phase).

Within the prior- β grains, very fine needle-like acicular martensite (α') phase was found in the as-built samples. The detailed description of α' formation in SLM Ti6Al4V can be found in [26,27,46]. After stress relieving, no difference is observed in the columnar morphology of prior- β grains, due to the fact that the stress-relieving heat treatment was carried out well below the β -transus temperature. The average prior- β grain width in stress-relieved samples is $90\pm 15\mu\text{m}$. However, a partial decomposition of α' is observed where α' started to transform to more stabilized $\alpha+\beta$ at the boundaries. However, it can be observed that a significant number of α' martensite needles are still embedded in the more stable $\alpha+\beta$.

3.3. Residual stresses

The contour method stress results are presented in three different groups. The first group presents the residual stress in the original build block; and the change in residual stress due to machining to a rectangular block, machining to the C(T) geometry, and stress-relieving by heat treatment. The second group compares the residual distribution in the sample with cracks grown parallel or across the build layers, i.e. ZX and XZ respectively as shown in figure 1. Finally, a comparison between neutron diffraction and contour method results is presented.

Interesting results were found when comparing the as-built un-machined block (Fig. 4a) with as-built machined without a notch (Fig 4b), and as-built machined C(T)

before and after stress relieving (Fig. 4c and 4d). In the former, most of the cross-sectional area is covered by large compressive stresses. Large thermal gradient coupled with low heat transfer between the layers has resulted in compressive stress of magnitude reaching up to -400 MPa. High tensile stresses reaching up to 750 MPa are found close to the sample edge along the X-axis of the vertical built block, while moderate tensile stresses of 300 MPa were found close to the sample edge along the mid Y-axis. The small variation in the stress at the centre of the sample is mainly associated with the difference in the cooling rate. The edges of the sample are exposed to the loose powder particles at their periphery, leading to a faster cooling rate through conduction and convection heat transfer. Hence, large tensile stresses were found on the edges compared to the middle. At the middle, only minimal heat transfer through conduction will take place, hence compressive stresses is observed.

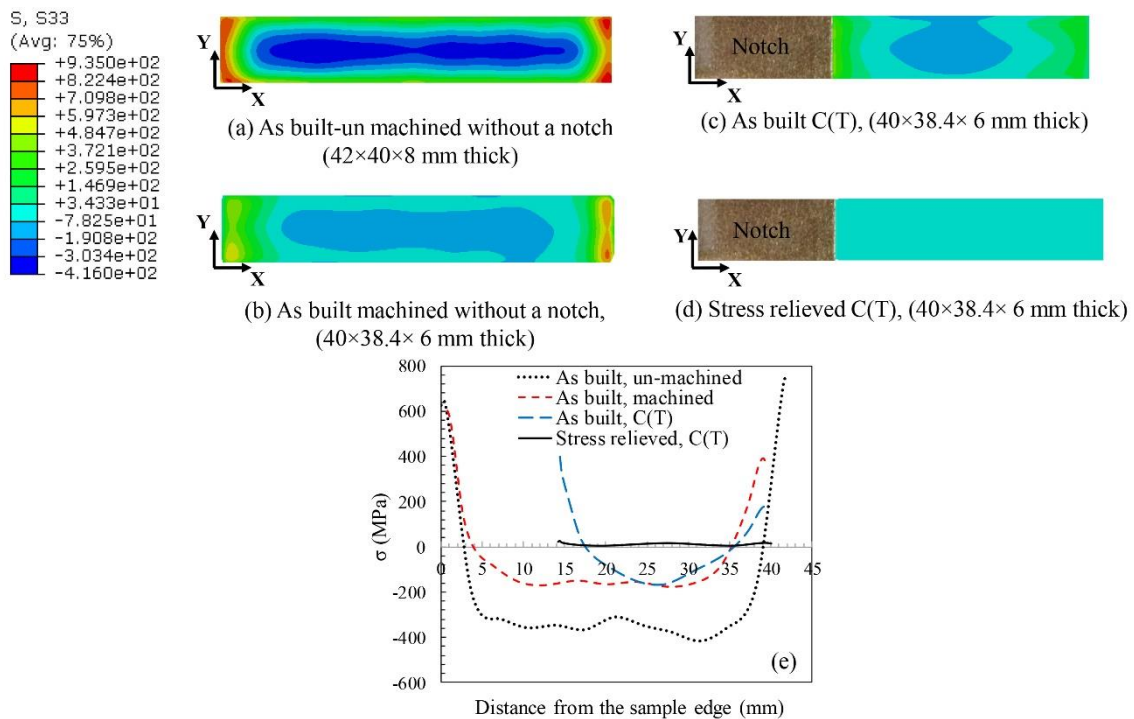


Fig. 4: Residual stress distributions in ZX sample measured using contour method: (a) as built un-machined, without a notch (8 mm thick), (b) as built machined, without a notch (6 mm thick), (c) as built C(T), 6 mm thick, (d) stress relieved C(T), 6 mm thick (e) stress line profiles for the samples in (a)-(d).

During the C(T) sample machining, the initial 8 mm thick block was reduced to 6 mm thickness using high-precision milling. Residual stresses were measured on this 6-mm-thick rectangular block before (without a notch) and after the C(T) sample

manufacturing. For this, the top, bottom, and sides of the build were skimmed. Residual stresses on the rectangular block without a notch are presented in Fig. 4b. After machining to a 6-mm-thick rectangular block, a maximum tensile stress of 600 MPa is found on the surfaces (of the shorter side of the cross-section) of the sample whereas a maximum compressive stress of -170 MPa is found in the middle. The machining process has relieved 20% and 55% of tensile and compressive stress respectively compared to the as-built un-machined condition.

After machining and introducing a notch, the maximum tensile and compressive stresses in the C(T) sample are 300 MPa and -160 MPa respectively. Stress redistribution was mainly caused by the notch introduction. The tensile stresses near the notch root and on the edge of the sample are diminished after the heat treatment, Fig. 4d. Negligible stresses (<20 MPa) are present throughout the sample. Fig. 4e shows stress line profiles for the samples in Fig 4 (a)-(d). From the contour method, it is evident that the machining process will cause considerable stress-relief, whereas heat treatment is very effective in relieving about 90% of residual stress developed during the SLM process.

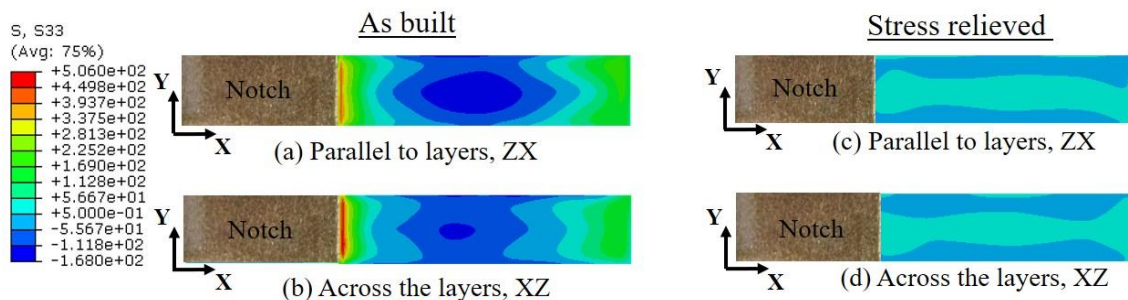


Fig. 5: Residual stress distribution in as-built and stress-relieved C(T) samples measured by the contour method. The measured stress component is perpendicular to the crack plane as shown in figure 1. (a) as built, crack parallel to layers, ZX orientation; (b) as built, crack across the layers, XZ orientation; (c) stress relieved, crack parallel to layers, ZX orientation; (d) stress relieved, crack across the layers, XZ orientation.

Fig. 5 shows the residual stress distribution on the crack growth plane in the as-built and stress-relieved samples. In the as-built condition, the residual stress distribution was found to be similar for both the vertically-built ZX and XZ samples. This agrees with previous work [18], although in that case the magnitude of the residual stresses was lower. This might be due to the thicker, smaller sample size used. Furthermore, the process

parameters, powder quality and particle size distribution will also influence the residual stress. High tensile stresses approaching 450-500 MPa were found close to the notch root in the as-built ZX and XZ samples.

A significant relaxation of residual stress was found after the stress-relieving heat treatment (Fig. 5c and 5d). After stress relieving, a maximum tensile stress of 30 MPa was measured, indicating a reduction in residual stress of over 90%.

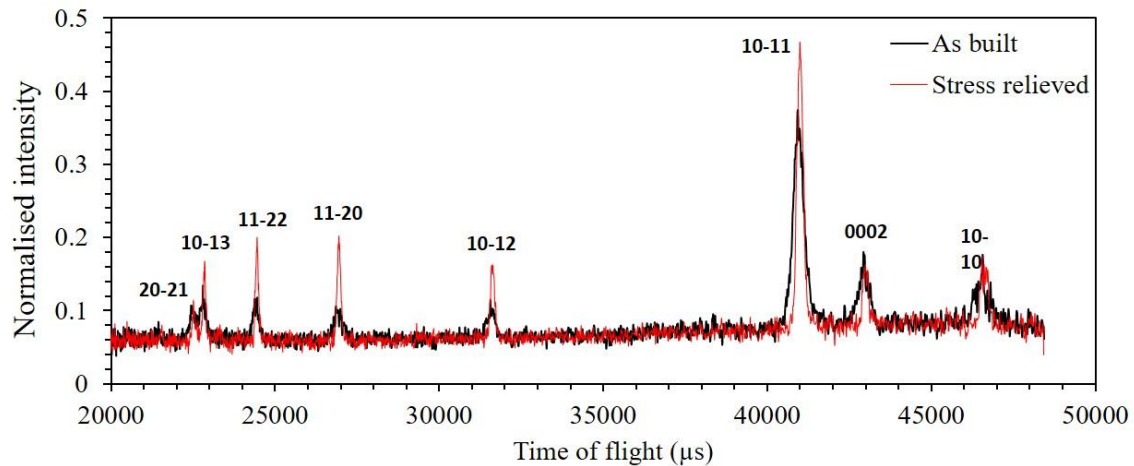


Fig. 6. Diffraction spectra of as-built and stress-relieved vertically-built ZX sample (see figure 1) at a distance of 11 mm from the notch root.

Residual strain measurement using neutron diffraction was performed only on the machined C(T) samples, and the results validated by comparing with the contour measurements. Typical neutron diffraction spectra obtained from the as-built and the stress-relieved C(T) samples are presented in Fig 6. The diffraction spectra showed only the presence of hexagonally-close-packed (HCP) α' martensite and the respective lattice planes are indicated. No β phase was found in either case. Among the diffraction peaks, the $\{10-11\}$ pyramidal plane shows the highest intensity.

Fig 7 (a)-(c) shows residual stresses in the as-built C(T) samples of two different planes with three different crack orientations. The transverse residual stress component (in the loading direction) is compared with the contour method for the vertical samples (ZX and XZ). For the horizontal build, as built XY sample has negligible tensile stresses close to the notch root (15 MPa) and on the edge of the sample in the transverse direction. Very low compressive stress of -16 MPa is observed at the centre of the sample in normal direction. Low tensile stresses in XY sample is attributed to its build height which is along the normal direction (N) with far fewer layers that results in fewer cycles of thermal

expansion and contraction and lower temperature gradient along the build, hence lower residual stresses.

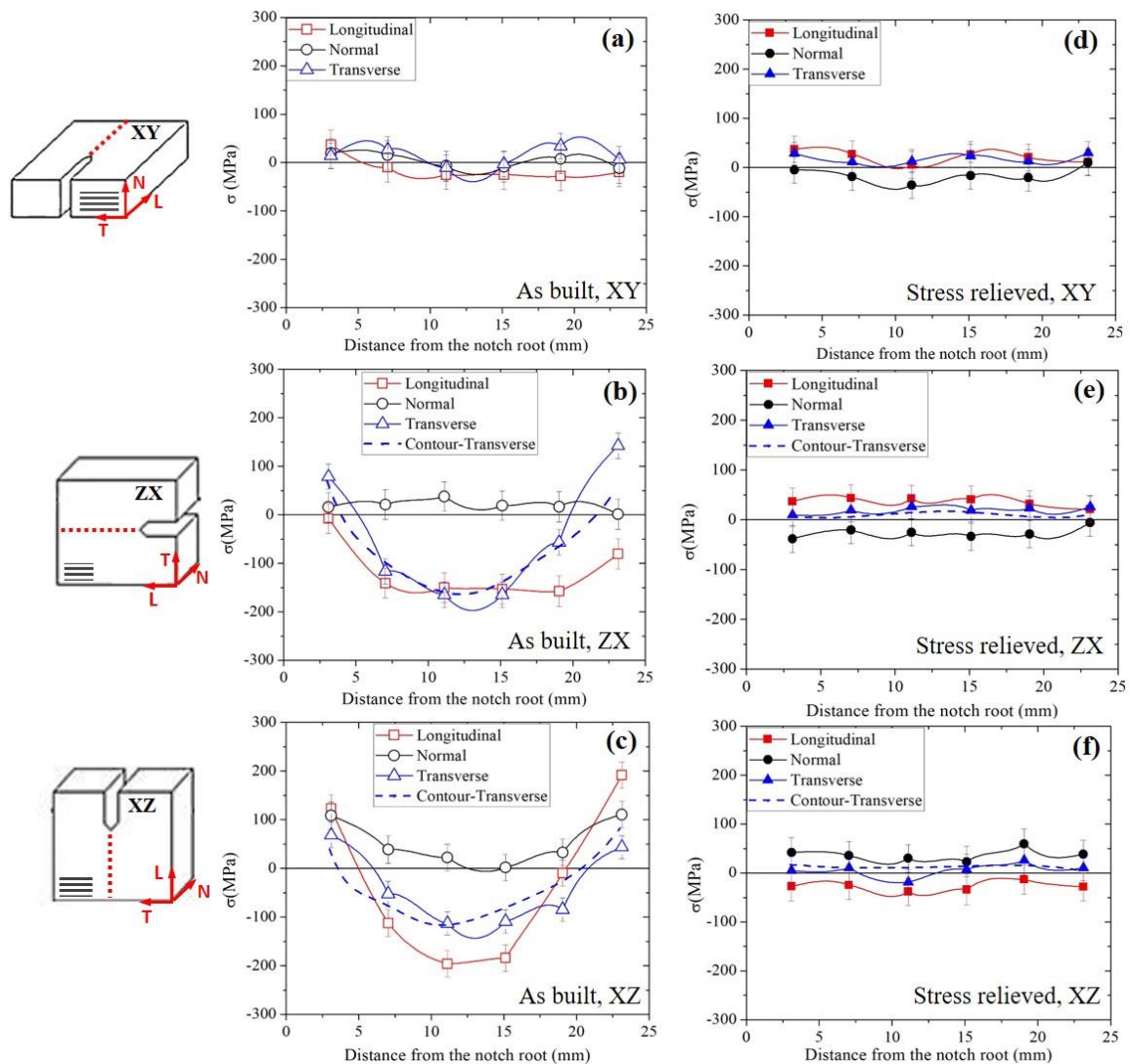


Fig. 7: Residual stresses in as-built and stress-relieved samples, measured by neutron diffraction, and compared with the contour method, for the transverse stress component.

For the vertical builds, ZX sample (crack across layers, Fig.7b), tensile stresses were found close to the notch root and at the edge of the sample in the transverse direction (which is the build and fatigue loading direction) and compressive stresses at the centre of the sample. Similar residual stress distribution pattern was observed in [17,18]. The large tensile stresses in ZX compared to XY are due to more number of thermal expansion and contraction cycles during the solidification process. Maximum tensile stress is observed in the transverse direction with a lower magnitude close to the notch root (80 MPa) compared to the far end of the sample (140 MPa). Whereas, balancing compressive

stresses exist in both the longitudinal and normal directions. The maximum compressive stresses of -165 MPa were found in the transverse direction. The magnitude of the compressive stresses is higher in the middle of the sample compared to the free edge, which is due to the faster heat dissipation and high solidification rate near the edge. The magnitude and the distribution of the compressive stresses may increase with an increase in the build height due to an increase in the number of thermal expansion and contraction cycles.

The neutron diffraction and contour measurements are in good agreement in terms of the transverse residual stress component. The contour results were plotted 3 mm away from the notch root, the same as neutron diffraction results, to aid better comparison. The small difference in the magnitude and distribution of the measured residual stresses between neutron and contour results is acceptable.

In the as-built vertical-build XZ sample (with the crack normal to the build layers)(see figure 1), tensile stresses are found close to the notch root and the edge of the sample in all three measured directions. The maximum tensile stresses are along the longitudinal direction (in the build plane) with 110 MPa close to the notch root and 190 MPa at the edge of the sample. In the transverse direction, tensile stresses of 65 MPa and 40 MPa are found close to the notch root and at the edge of the sample. A maximum compressive stress of -120 MPa is observed in the center of the sample along the transverse direction. A similar residual stress distribution was observed in [17,18]. The difference between the magnitude of the residual stresses reported in [18] and this research may be attributed to the difference in the build process parameters and the overall build size. From Fig. 7c, it can be observed that the contour results are in good agreement with neutron diffraction measurements.

Fig 7 (d)-(f) presents the residual stresses in the stress-relieved samples, demonstrating the benefits that are a consequence of stress-relief heat-treatment. Stress relieving did not result a significant change in residual stress distribution in the horizontal-build XY sample, as there was very little stress present initially. In the vertical-build ZX sample (Fig.7e), a significant reduction in residual stress is observed after the stress relieving heat treatment. Furthermore, compressive stresses were also reduced significantly. More than 90% of the tensile stresses are reduced after stress relieving.

From Fig.7e, it is again evident that the contour results are in very good agreement and confirm the neutron diffraction results.

The significant change in magnitude and stress distribution after stress relieving is coupled with a considerable decrease in full width half maximum (FWHM) and an increase in diffraction peak intensity (see Fig. 6). The change in FWHM and intensity after stress relieving is mainly due to a noticeable increase in α lath width compared to the as-built condition. Due to elemental partitioning, the partial decomposition of α' martensite present in the as-built condition transforms to more stable α after stress relieving. The α' martensite is a supersaturated phase in β stabilizing elements, whereas α is more stable and is not a supersaturated phase. All the stress-relieved samples showed similar diffraction patterns. Fig. 8a and 8b shows the change in FWHM and intensity of the $\{10-11\}$ plane in as-built and stress-relieved conditions for the vertically-built ZX and XZ samples, respectively. For both the samples, alongside the shift in the peak reflecting the strain relief, a considerable decrease in FWHM and increase in intensity is observed after stress relieving.

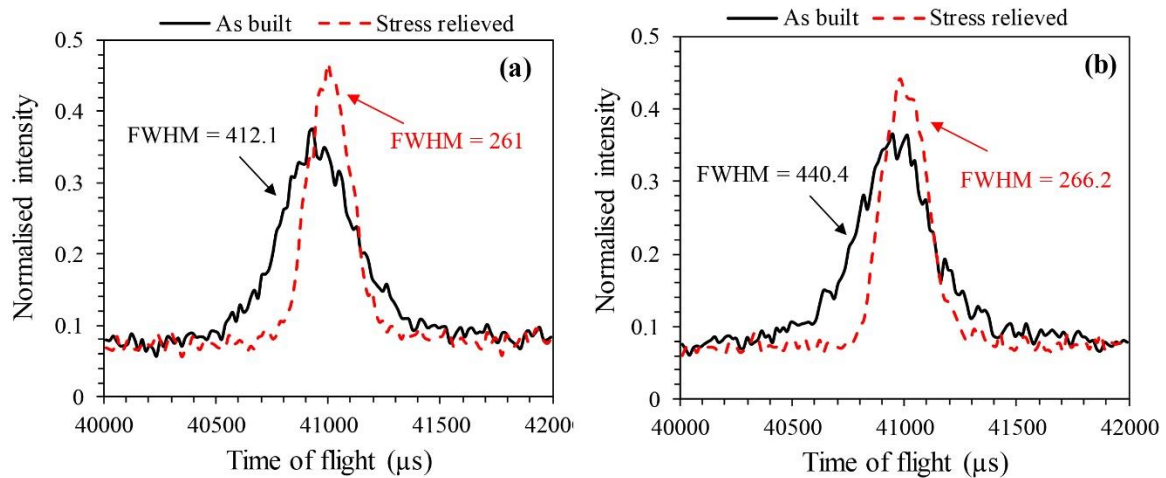


Fig. 8. Diffraction peak of $\{10-11\}$ plane for the vertically-built (see figure 1) (a) ZX (b) XZ samples in as-built and stress-relieved conditions. The $\{10-11\}$ has the highest intensity in the diffraction spectra.

Similarly, the XZ sample (also a vertical build, see figure 1) showed significant reduction in the residual stress after stress relief. Again, the contour results are in good agreement with the neutron diffraction results (refer Fig. 7f).

3.4. Fatigue crack growth

Although the same microstructural constituents are present in all the as-built samples, different crack orientations, and hence different microstructure with respect to the crack path, and the magnitude and distribution of residual stress, can be expected to affect fatigue crack growth behaviour. The difference in fatigue crack growth rate in as-built and stress-relieved samples can be seen in Fig. 9. The data presented are the average of three tests in each case, and are compared with traditionally processed Ti6Al4V: cast, β -annealed, and mill-annealed. The presence of residual stress and needle-like α' martensite has resulted in overall higher fatigue crack growth rate in the vertical-build as-built samples, compared to cast, β -annealed and wrought Ti6Al4V. The lower crack growth rate for cast, β -annealed and wrought materials compared to SLM Ti6Al4V is due to the absence of residual stresses. The horizontal built XY sample (see Fig. 1) showed lower crack growth rate compared to vertically built ZX and XZ: in the horizontal built XY samples, negligible residual stresses (10 MPa) are present at the notch root along the loading direction, compared to considerable tensile stresses of 80 MPa and 65 MPa in vertical built ZX and XZ samples respectively.

It is well documented that residual stress effects on fatigue crack growth rate can be accounted for by the residual stress intensity factor K_{res} . Tensile residual stress produces a positive K_{res} , and conversely compressive residual stress produce a negative K_{res} . Although presence of residual stress will not change the applied stress intensity range, it will change the applied stress intensity factor ratio R .

According to linear-elastic fracture mechanics, the effective stress intensity factor ratio in the presence of residual stress can be written as

$$R_{eff} = (K_{min} + K_{res}) / (K_{max} + K_{res}) \quad (3)$$

where K_{max} and K_{min} are maximum and minimum stress intensity factors.

A positive K_{res} thus increases R_{eff} and fatigue crack growth rate, and a negative K_{res} decreases R_{eff} . If the compressive residual stresses are sufficiently large enough, a negative R_{eff} implies crack closure.

Although tensile stresses are present at the notch root of ZX sample, a large portion of the crack path has compressive residual stress (Fig. 7). One would expect that the presence of compressive residual stresses at the centre of the sample will slow the crack growth rate. Research performed in [18,35] showed similar compressive stresses in

the centre of the sample. However, they have also shown tensile stresses (up to 200 MPa) near the edges. So whilst compressive stresses in the centre may contribute to reducing the applied K_{max} , the large tensile residual stresses near the lateral edges (free surfaces) of the crack plane will substantially add to the applied K_{max} , thereby giving rise to an increase in crack growth rate as the crack advances through the compressive stress field. Furthermore, recent studies performed in [13] observed an effect where the crack is longer close to the free surfaces compared to the sample centre-line. This is indicating that the crack is propagating at a slower rate in the centre of the sample (possibly owing to the compressive residual stresses) compared to the free surface. In the current study, as the crack length was measured on the free surface only, the ZX sample showed a higher crack growth rate. However, the samples used in the current study were thinner compared to [13], and the surface effect will have higher dominance as a result.

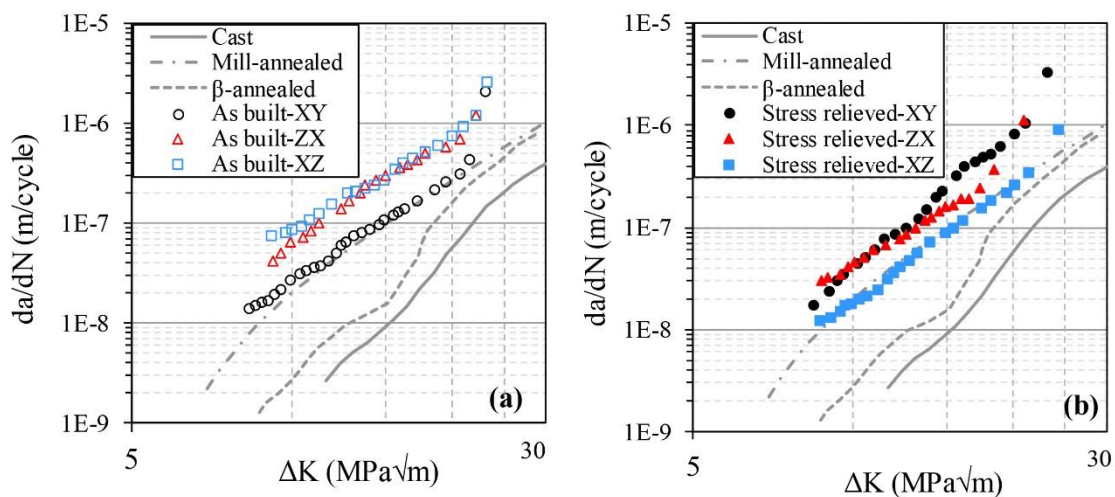


Fig. 9. Average fatigue crack growth rate curves for (a) as-built (b) stress-relieved samples

If we analyse the crack propagation with respect to the microstructural directionality (*i.e.*, the columnar prior- β grain orientation), the crack propagates perpendicular to the deposition direction and parallel to the columnar prior β grain orientation in the vertical-build XZ sample (see figure 1). As a result, the crack propagates along the prior- β grain boundaries with limited interaction with the prior- β grain itself, and this results in faster crack growth rate. Other studies conducted on fatigue crack growth of SLM Ti6Al4V also detected higher crack growth rates in samples with the crack propagation direction parallel to the columnar prior- β grains [13,18]. The effect of columnar β grain orientation on the crack propagation can only be observed during the

initial crack propagation period (*i.e.*, up to 11 MPa \sqrt{m}). After 11 MPa \sqrt{m} , no significant difference in crack growth rate between the ZX and XZ samples is observed, Fig 9. At a given stress intensity range (for example at $\Delta K=15\text{MPa}\sqrt{m}$) in the as-built condition, the horizontal-build XY samples (see figure 1) show 15-20% lower crack growth rate compared to the ZX and XZ samples. Overall, in the as-built condition, the crack growth rate is governed by residual stresses and the microstructure.

Stress relieving by heat treatment has resulted in a significant reduction in residual stress magnitude compared to the as-built condition (Fig. 7). Overall, the horizontal-build XY sample shows the highest crack growth rate after stress relieving, followed by ZX and XZ samples. Of the vertical-build samples (see figure 1), the ZX sample shows higher crack growth rate compared to XZ. Here, the microstructure is expected to play a major role in the crack initiation and crack growth. A considerable variation in crack growth rate between ZX (crack propagating along the build layers) and XZ (crack propagating across the layers) is observed until 15MPa \sqrt{m} , after which no considerable variation is found, Fig 10. Stress relieved ZX sample-3 show two different slopes in the da/dN vs ΔK and da/dN vs crack length curve, indicating two different crack growth rate regimes. In the first regime (up to 15MPa \sqrt{m}), the slope of the curve is lower indicating lower crack growth rate. This is due to the crack is growing perpendicular to the columnar prior β grains and repeatedly passing through the α_{GB} causing more resistance on the crack growth. Hence, a lower crack growth rate is observed. However, once the crack reached ΔK of 15MPa \sqrt{m} the columnar prior β grains did not play any role to resist the crack growth. Hence, increased crack growth rate is observed after ΔK of 15MPa \sqrt{m} . The higher crack growth rate in the XY sample is likely due to the presence of small tensile stresses close to the notch root.

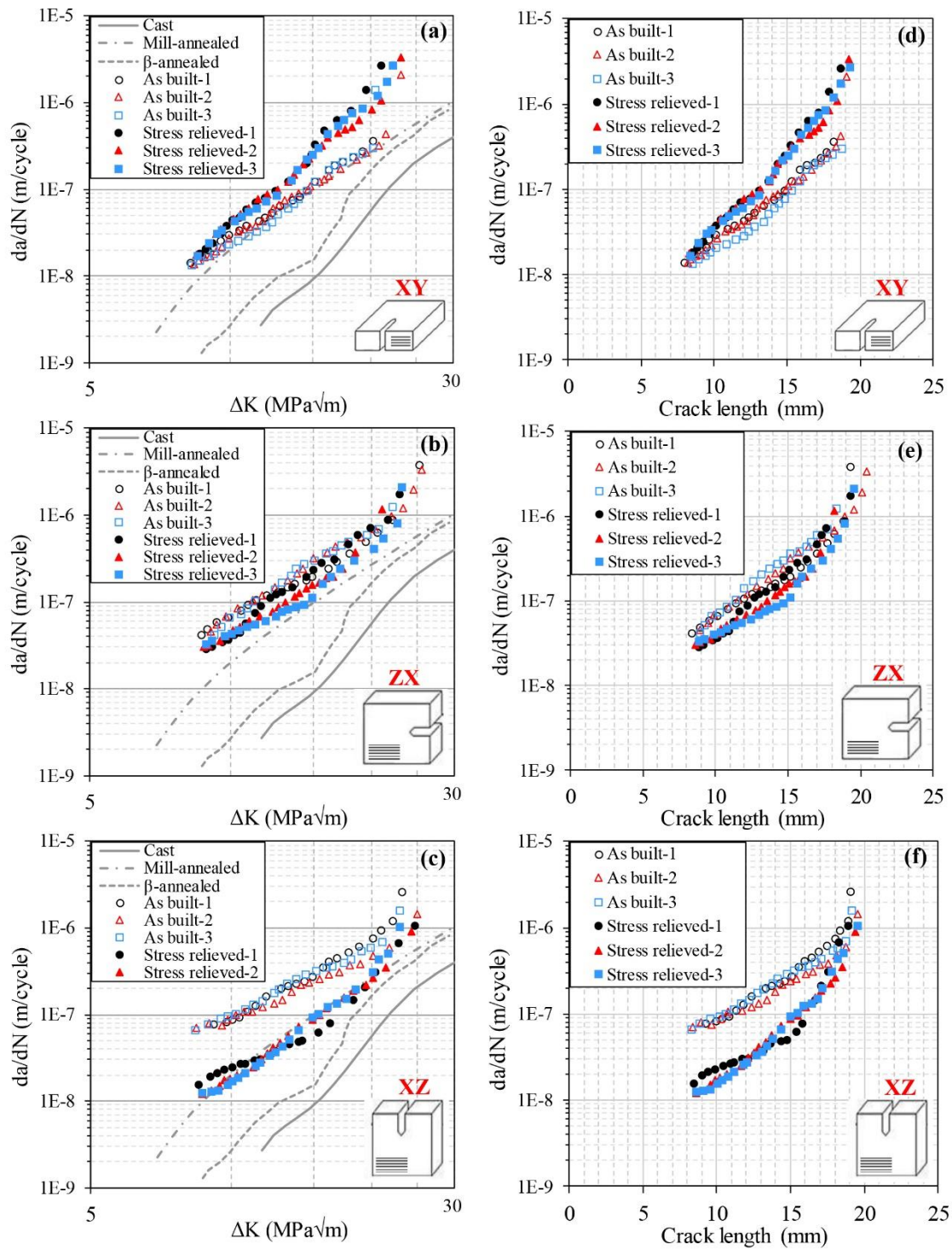


Fig. 10. Fatigue crack growth rate curves for as-built and stress-relieved samples (a)-(c) da/dN vs ΔK for XY, ZX, and XZ orientations respectively (see figure 1). (d)-(f) da/dN vs crack length for XY, ZX, and XZ orientations respectively

Fig. 10 d-f present fatigue crack growth rate, da/dN , as a function of crack length in the as-built and stress-relieved condition for the three orientations. Horizontal-build XY sample showed a small increase in crack growth rate after stress relieving compared to the as-built condition. Lower tensile stresses in the as-built condition close to the notch root and small compressive stresses after 8 mm from the notch root cumulatively resulted lower crack growth rate compared to stress relieved condition in all three tests.

For the vertical-build ZX sample (see figure 1), tensile stresses close to the notch root in the as-built condition result in higher fatigue crack growth rate. When the crack reaches the maximum compressive stress field (*i.e.*, at 12 mm crack length), the crack growth rate is reduced in the as-built condition, as seen by change the change in slope after 12 mm crack length in Fig. 10e. After 12 mm crack length, similar crack growth rate is observed in as-built and stress-relieved ZX samples. On the other hand, the compressive residual stress of -120 MPa in the middle of the as-built XZ sample did not contribute to reduce the crack growth rate. Once the crack initiated, the crack growth rate is controlled by the crack propagation with respect to the microstructural directionality (*i.e.* columnar prior β grain orientation). The crack propagates parallel to the columnar prior β grain orientation in XZ. As a result, the crack propagates along the prior β grain boundaries with limited interaction with the prior β grain itself and results in faster crack growth rate.

3.5. Fractography analysis

Fracture samples showing crack path profiles are presented in Fig. 11a. Except for the as-built sample with the crack across the build layers (XZ, see figure 1), all samples show a straight crack path. The as-built XZ sample showed crack deviation from an early stage of crack propagation. The crack was inclined about 13° to the notch. To understand the microstructural mechanism of crack deviation, optical microscopy was carried on a large area of as-built ZX and XZ samples, as both were cut from the same plane but had different notch orientation with respect to the prior- β grain orientation. The relative orientation of columnar prior- β grains at the crack tip determines the crack path. Optical micrographs of the crack path are presented in Fig. 11b, where the crack is propagating through prior- β grains in the ZX sample and parallel to prior- β grains in the XZ samples.

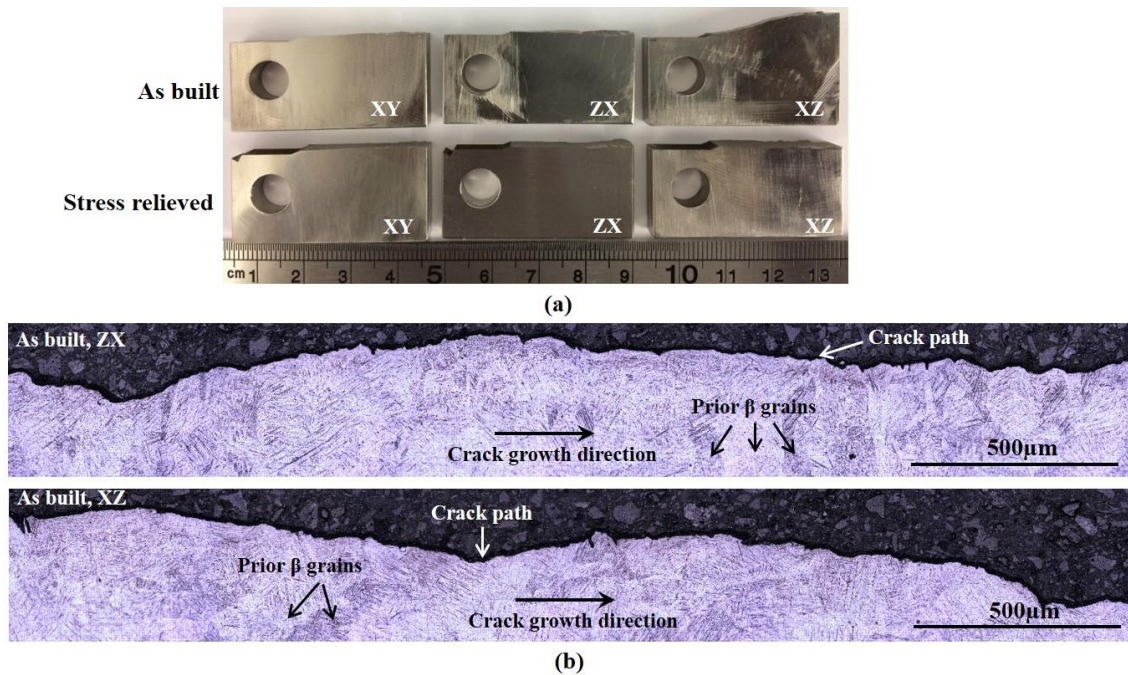


Fig .11. (a) Photograph showing crack path in as-built and stress-relieved samples. (b) Optical micrograph showing crack passing across prior- β grains (ZX) and along the prior β grains in (XZ) samples. Crack growth direction is from left to the right of the image.

Although crack deviation is observed in the XZ samples (Fig. 11a), the optical micrographs shown in Fig. 11b did not show any concrete evidence on the crack deviation mechanism. Samples consists of a very fine acicular α' microstructure which made the quantification of the crack deviation mechanism with respect to the microstructural features challenging. However, previous studies [47,48] on additive-manufactured Ti6Al4V have shown that crack propagation parallel to the prior- β grains resulted in significant crack branching. It was concluded in [47,48] that the crack propagation perpendicular to the prior- β grains (ZX orientation, see figure 1) causes the crack to cut through the prior- β grain boundaries, resulting in a straight crack path. Whereas, in samples with the crack parallel to the prior- β grains (XZ orientation), the prior- β grain boundary acts as the crack deflector in angles close to their orientation, leading to crack deviation. A similar hypothesis can be made here, where both the columnar grain structure and each deposited layer contributed to crack deviation in the XZ samples.

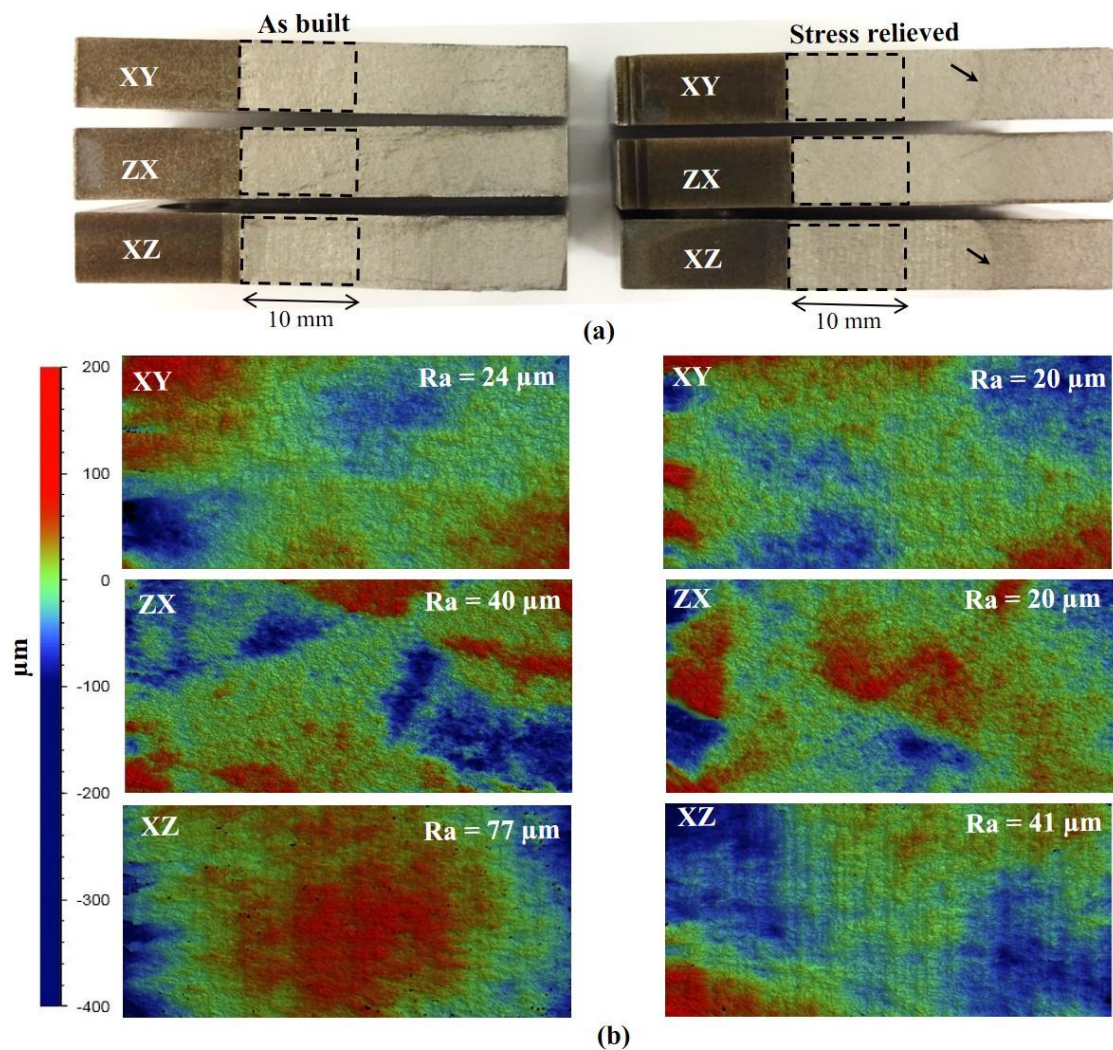


Fig. 12. Fractography images showing (a) fracture surfaces for as-built and stress-relieved samples (b) fracture surface roughness maps obtained from the interferometer.

The location and area of the surface roughness maps are highlighted with dotted rectangular box in Fig 12(a). The crack growth direction is from left to the right of the image.

Fracture surfaces of as-built and stress-relieved samples are shown in Fig 12a. The fracture surfaces show the difference between the fatigue crack growth and fast fracture regions, though this is more evident in the stress-relieved samples. The fatigue crack fronts before fast fracture for the stress-relieved samples are highlighted with an arrow in Fig 12a. Surface roughness maps of the fracture surfaces in the crack growth region are shown in figure 12b. From the surface roughness maps, it was found that the horizontal-build XY sample (see figure 1) shows lowest average surface roughness ($R_a = 24\mu\text{m}$), the XZ sample shows highest average surface roughness, and the ZX sample lies in-

between. Lower fracture surface roughness of XY sample is associated with low residual stress and a crack path perpendicular to the columnar grains. The crack interaction with columnar β grain boundaries leads to a rougher fracture surface ($R_a = 77\mu\text{m}$) in the XZ samples, resulting in crack deviation that has contributed to large tortuosity (a measure of deviation from its straight path) of the crack where more energy required to extend the crack nominal to crack plane [47,49]. The ZX sample shows moderate fracture surface roughness ($R_a = 40\mu\text{m}$), as the crack propagated through the prior- β grains resulting in lower crack deviation and less tortuosity. After stress relieving, all the samples show a reduction of fracture surface roughness, most pronounced in the ZX and XZ samples. The flat topography of the stress-relieved samples can also be observed from Fig 12a.

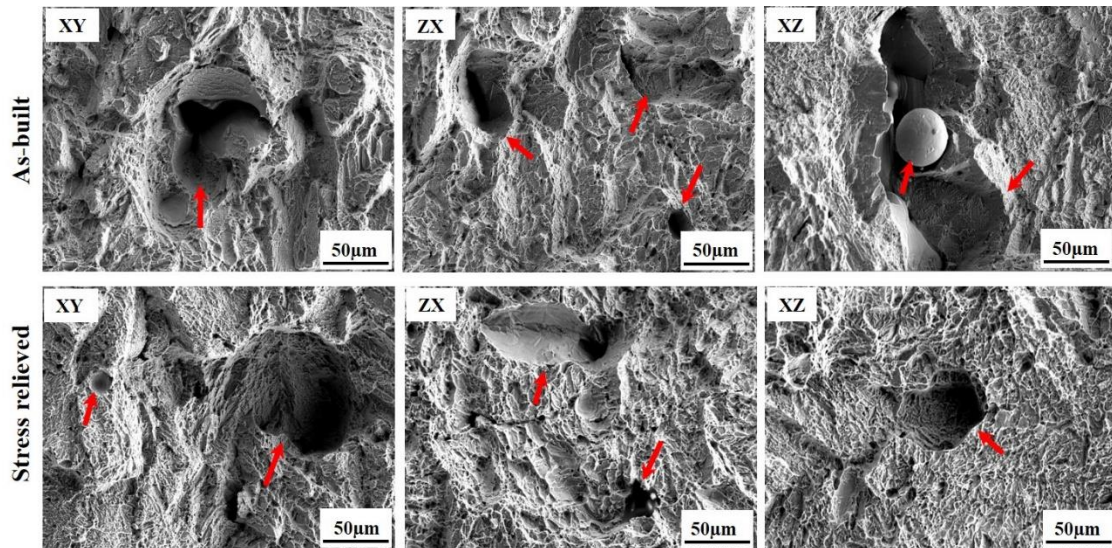


Fig. 13. Secondary electron SEM images of the fracture surfaces, revealing the presence of gas pores and lack-of-fusion pores can be observed that are highlighted with arrows.

Partially melted powder particles can also be observed.

Fig. 13 shows secondary electron SEM images showing fracture surfaces of as-built and stress-relieved samples. The crack growth direction is from left to right of each image. All the samples have similar fatigue fracture mechanism with a transgranular fracture. Very fine ridges appearing on the fracture surfaces were formed due to the interaction of crack with very fine α' laths. Fracture surfaces also revealed both gas pores and lack-of-fusion pores in both crack growth and final fracture regions.

Conclusions

Microstructure, residual stress and fatigue crack growth behaviour of as-built and stress-relieved Ti6Al4V samples fabricated by selective laser melting (SLM) have been investigated, and the following conclusions can be drawn.

1. The as-built microstructure consists of epitaxially grown prior- β grains aligned parallel to the build direction. Within the prior- β grains, very fine needle-like acicular martensite (α') phase is observed. After stress relieving, a partial decomposition of α' martensite is observed, and the α' transformed to more stabilized $\alpha+\beta$. Porosity was found with a pore size ranging from 5-34 μm in both as-built and stress-relieved samples.
2. In samples built vertically from the base plate (see Fig. 1 for a schematic), high values of residual stress were seen, with highest values approaching 600 MPa tension near the surface and -400 compression in the centre of the samples in the initial as-built condition. Building the samples horizontally (effectively “flat” on the base plate, see Fig. 1), resulted in negligible residual stress as a result of the small number of SLM layers deposited to build the samples. After stress relieving, low residual stress was seen in all samples. There was good agreement with the residual stress data obtained using neutron diffraction and the contour method.
3. The lower residual stress in the horizontal-build samples resulted in a lower crack growth rate compared to the vertical build, in the as-built condition.
4. After stress relieving, residual stresses were insignificant, and the crack growth rate is driven by the orientation of the crack growth relative to the microstructure. Fatigue crack propagates parallel to the columnar prior β grains have limited interaction with the prior β grain itself and results in faster crack growth rate compared to the crack propagates perpendicular to the prior β grains.
5. Overall, it is observed that the residual stresses are a major factor influencing the fatigue crack behaviour of SLM Ti6Al4V. In order to minimise process-induced residual stresses, it is advised that the material/part should be built with the lowest possible height from the base plate. If a “tall” part geometry is required, a stress-relieving heat treatment is advised to minimise the residual stresses and enhance the fatigue crack growth performance.

Acknowledgements

Dr Joe Kelleher, instrument scientist at ENGIN-X, ISIS facility, UK is acknowledged for his support during the residual strain measurements. We also thank Ian Wilson, Steve Damms and Barry Meek for their support on sample manufacturing. MEF is grateful for funding from the Lloyd's Register Foundation, a charitable foundation helping to protect life and property by supporting engineering-related education, public engagement and the application of research.

References

- [1] L. Christoph, P. Manfred, eds., *Titanium and Titanium Alloys: Fundamentals and Applications*, Wiley-VCH Verlag GmbH & Co. KGaA, 2005.
- [2] Vydehi Arun Joshi, *Titanium Alloys: An Atlas of Structures and Fracture Features*, CRC Press, 2006.
- [3] B. Dutta, F.H. Froes, Additive manufacturing of titanium alloys, *Adv. Mater. Process.* 172 (2014) 18–23. doi:10.4028/www.scientific.net/AMR.1019.19.
- [4] E. Louvis, P. Fox, C.J. Sutcliffe, Selective laser melting of aluminium components, *J. Mater. Process. Technol.* 211 (2011) 275–284. doi:10.1016/J.JMATPROTEC.2010.09.019.
- [5] E.O. Olakanmi, R.F. Cochrane, K.W. Dalgarno, A review on selective laser sintering/melting (SLS/SLM) of aluminium alloy powders: Processing, microstructure, and properties, *Prog. Mater. Sci.* 74 (2015) 401–477. doi:10.1016/J.PMATSCI.2015.03.002.
- [6] D. Zhang, W. Niu, X. Cao, Z. Liu, Effect of standard heat treatment on the microstructure and mechanical properties of selective laser melting manufactured Inconel 718 superalloy, *Mater. Sci. Eng. A.* 644 (2015) 32–40. doi:10.1016/j.msea.2015.06.021.
- [7] L.N. Carter, K. Essa, M.M. Attallah, Optimisation of selective laser melting for a high temperature Ni-superalloy, *Rapid Prototyp. J.* 21 (2015) 423–432. doi:10.1108/RPJ-06-2013-0063.
- [8] N.J. Harrison, I. Todd, K. Mumtaz, Reduction of micro-cracking in nickel superalloys processed by Selective Laser Melting: A fundamental alloy design approach, *Acta Mater.* 94 (2015) 59–68. doi:10.1016/j.actamat.2015.04.035.
- [9] K. Abd-Elghany, D.L. Bourell, Property evaluation of 304L stainless steel

- fabricated by selective laser melting, *Rapid Prototyp. J.* 18 (2012) 420–428.
doi:10.1108/13552541211250418.
- [10] L. Thijs, F. Verhaeghe, T. Craeghs, J. Van Humbeeck, J.-P.P. Kruth, A study of the microstructural evolution during selective laser melting of Ti-6Al-4V, *Acta Mater.* 58 (2010) 3303–3312. doi:10.1016/j.actamat.2010.02.004.
- [11] W. Xu, M. Brandt, S. Sun, J. Elambasseril, Q. Liu, K. Latham, K. Xia, M. Qian, Additive manufacturing of strong and ductile Ti–6Al–4V by selective laser melting via in situ martensite decomposition, *Acta Mater.* 85 (2015) 74–84. doi:10.1016/j.actamat.2014.11.028.
- [12] B. Vrancken, L. Thijs, J.P. Kruth, J. Van Humbeeck, Microstructure and mechanical properties of a novel β titanium metallic composite by selective laser melting, *Acta Mater.* 68 (2014) 150–158. doi:10.1016/j.actamat.2014.01.018.
- [13] V. Cain, L. Thijs, J. Van Humbeeck, B. Van Hooreweder, R. Knutsen, Crack propagation and fracture toughness of Ti6Al4V alloy produced by selective laser melting, *Addit. Manuf.* 5 (2015) 68–76. doi:10.1016/j.addma.2014.12.006.
- [14] T. Vilaro, C. Colin, J.D. Bartout, As-fabricated and heat-treated microstructures of the Ti-6Al-4V alloy processed by selective laser melting, *Metall. Mater. Trans. A Phys. Metall. Mater. Sci.* 42 (2011) 3190–3199. doi:10.1007/s11661-011-0731-y.
- [15] M. Simonelli, Y.Y. Tse, C. Tuck, Effect of the build orientation on the mechanical properties and fracture modes of SLM Ti-6Al-4V, *Mater. Sci. Eng. A.* 616 (2014) 1–11. doi:10.1016/j.msea.2014.07.086.
- [16] L. Thijs, M.L. Montero Sistiaga, R. Wauthle, Q. Xie, J.-P. Kruth, J. Van Humbeeck, Strong morphological and crystallographic texture and resulting yield strength anisotropy in selective laser melted tantalum, *Acta Mater.* 61 (2013) 4657–4668. doi:10.1016/j.actamat.2013.04.036.
- [17] P. Mercelis, J. Kruth, Residual stresses in selective laser sintering and selective laser melting, *Rapid Prototyp. J.* 12 (2006) 254–265.
doi:10.1108/13552540610707013.
- [18] B. Vrancken, V. Cain, R. Knutsen, J. Van Humbeeck, Residual stress via the contour method in compact tension specimens produced via selective laser melting, *Scr. Mater.* 87 (2014) 29–32. doi:10.1016/j.scriptamat.2014.05.016.

- [19] J.-P. Kruth, J. Deckers, E. Yasa, R. Wauthlé, Assessing and comparing influencing factors of residual stresses in selective laser melting using a novel analysis method, *Proc. Inst. Mech. Eng. Part B J. Eng. Manuf.* 226 (2012) 980–991. doi:10.1177/0954405412437085.
- [20] Y. Liu, Y. Yang, D. Wang, A study on the residual stress during selective laser melting (SLM) of metallic powder, *Int. J. Adv. Manuf. Technol.* 87 (2016) 647–656. doi:10.1007/s00170-016-8466-y.
- [21] B. Vrancken, R. Wauthle, J. Kruth, J. Van Humbeeck, Study of the Influence of Material Properties on Residual Stress in Selective Laser Melting, *Proc. 24th Int. Solid Free. Fabr. Symp.* (2013) 393–407.
- [22] L. Parry, I.A. Ashcroft, R.D. Wildman, Understanding the effect of laser scan strategy on residual stress in selective laser melting through thermo-mechanical simulation, *Addit. Manuf.* 12 (2016) 1–15. doi:10.1016/j.addma.2016.05.014.
- [23] P.A. Kobryn, S.L. Semiatin, The laser additive manufacture of Ti-6Al-4V, *JOM.* 53 (2001) 40–42. doi:10.1007/s11837-001-0068-x.
- [24] L. Facchini, E. Magalini, P. Robotti, A. Molinari, S. Höges, K. Wissenbach, Ductility of a Ti-6Al-4V alloy produced by selective laser melting of prealloyed powders, *Rapid Prototyp. J.* 16 (2010) 450–459. doi:10.1108/13552541011083371.
- [25] P.A. Kobryn, E.H. Moore, S.L. Semiatin, Effect of laser power and traverse speed on microstructure, porosity, and build height in laser-deposited Ti-6Al-4V, *Scr. Mater.* 43 (2000) 299–305. doi:10.1016/S1359-6462(00)00408-5.
- [26] C. Qiu, N.J.E. Adkins, M.M. Attallah, Microstructure and tensile properties of selectively laser-melted and of HIPed laser-melted Ti-6Al-4V, *Mater. Sci. Eng. A.* 578 (2013) 230–239. doi:10.1016/j.msea.2013.04.099.
- [27] J. Yang, H. Yu, J. Yin, M. Gao, Z. Wang, X. Zeng, Formation and control of martensite in Ti-6Al-4V alloy produced by selective laser melting, *Mater. Des.* 108 (2016) 308–318. doi:10.1016/j.matdes.2016.06.117.
- [28] J. Yang, H. Yang, H. Yu, Z. Wang, H. Wang, X. Zeng, A novel approach to in-situ fabricate Ti-6Al-4V alloy with graded microstructure and property by selective laser melting, *Mater. Lett.* 215 (2018) 246–249. doi:10.1016/J.MATLET.2017.12.098.

- [29] H. Wan, Q. Wang, C. Jia, Z. Zhang, Multi-scale damage mechanics method for fatigue life prediction of additive manufacture structures of Ti-6Al-4V, *Mater. Sci. Eng. A.* 669 (2016) 269–278. doi:10.1016/j.msea.2016.05.073.
- [30] S. Tammas-Williams, P.J. Withers, I. Todd, P.B. Prangnell, The Influence of Porosity on Fatigue Crack Initiation in Additively Manufactured Titanium Components, *Sci. Rep.* 7 (2017) 7308. doi:10.1038/s41598-017-06504-5.
- [31] M. Simonelli, Microstructure Evolution and Mechanical Properties of Selective Laser Melted Ti-6Al-4V, (2014).
- [32] B. Van Hooreweder, R. Boonen, D. Moens, J.-P. Kruth, P. Sas, On the determination of fatigue properties of Ti6Al4V produced by selective laser melting, in: 53rd AIAA/ASME/ASCE/AHS/ASC Struct. Struct. Dyn. Mater. Conf., American Institute of Aeronautics and Astronautics, 2012. doi:doi:10.2514/6.2012-1733.
- [33] A.H. Nickel, D.M. Barnett, F.B. Prinz, Thermal stresses and deposition patterns in layered manufacturing, *Mater. Sci. Eng. A.* 317 (2001) 59–64. doi:10.1016/S0921-5093(01)01179-0.
- [34] M.F. Zaeh, G. Branner, Investigations on residual stresses and deformations in selective laser melting, *Prod. Eng.* 4 (2010) 35–45. doi:10.1007/s11740-009-0192-y.
- [35] P. Rangaswamy, M.L. Griffith, M.B. Prime, T.M. Holden, R.B. Rogge, J.M. Edwards, R.J. Sebring, Residual stresses in LENS components using neutron diffraction and contour method, *Mater. Sci. Eng. A.* 399 (2005) 72–83. doi:10.1016/j.msea.2005.02.019.
- [36] P. Edwards, M. Ramulu, Fatigue performance evaluation of selective laser melted Ti-6Al-4V, *Mater. Sci. Eng. A.* 598 (2014) 327–337. doi:10.1016/j.msea.2014.01.041.
- [37] P. Edwards, M. Ramulu, Effect of build direction on the fracture toughness and fatigue crack growth in selective laser melted Ti-6Al-4-??V, *Fatigue Fract. Eng. Mater. Struct.* 38 (2015) 1228–1236. doi:10.1111/ffe.12303.
- [38] J.R. Santisteban, M.R. Daymond, J.A. James, L. Edwards, ENGIN-X: a third-generation neutron strain scanner, *J. Appl. Crystallogr.* 39 (2006) 812–825. doi:10.1107/S0021889806042245.

- [39] M.B. Prime, Cross-Sectional Mapping of Residual Stresses by Measuring the Surface Contour After a Cut, *J. Eng. Mater. Technol.* 123 (2000) 162–168.
<http://dx.doi.org/10.1115/1.1345526>.
- [40] N. Hrabe, T. Gnaupel-Herold, T. Quinn, Fatigue properties of a titanium alloy (Ti-6Al-4V) fabricated via electron beam melting (EBM): Effects of internal defects and residual stress, *Int. J. Fatigue.* 94 (2017) 202–210.
[doi:10.1016/j.ijfatigue.2016.04.022](https://doi.org/10.1016/j.ijfatigue.2016.04.022).
- [41] H. Gong, H. Gu, K. Zeng, J.J.. Dilip, D. Pal, B. Stucker, D. Christiansen, J. Beuth, J.. Lewandowski, Melt pool characterization for selective laser melting of Ti-6Al-4V pre-alloyed powder, in: 25th Annu. Int. Solid Free. Fabr. Symp., 2014: pp. 256–67.
- [42] A. Safdar, L.Y. Wei, A. Snis, Z. Lai, Evaluation of microstructural development in electron beam melted Ti-6Al-4V, *Mater. Charact.* 65 (2012) 8–15.
[doi:10.1016/j.matchar.2011.12.008](https://doi.org/10.1016/j.matchar.2011.12.008).
- [43] C. de Formanoir, S. Michotte, O. Rigo, L. Germain, S. Godet, Electron beam melted Ti-6Al-4V: Microstructure, texture and mechanical behavior of the as-built and heat-treated material, *Mater. Sci. Eng. A.* 652 (2016) 105–119.
[doi:10.1016/j.msea.2015.11.052](https://doi.org/10.1016/j.msea.2015.11.052).
- [44] L. Qian, J. Mei, J. Liang, X. Wu, Influence of position and laser power on thermal history and microstructure of direct laser fabricated Ti-6Al-4V samples, *Mater. Sci. Technol.* 21 (2005) 597–605. [doi:10.1179/174328405X21003](https://doi.org/10.1179/174328405X21003).
- [45] X. Wu, J. Liang, J. Mei, C. Mitchell, P.S. Goodwin, W. Voice, Microstructures of laser-deposited Ti-6Al-4V, *Mater. Des.* 25 (2004) 137–144.
[doi:10.1016/j.matdes.2003.09.009](https://doi.org/10.1016/j.matdes.2003.09.009).
- [46] B. Vrancken, L. Thijs, J.-P. Kruth, J. Van Humbeeck, Heat treatment of Ti6Al4V produced by selective laser melting: microstructure and mechanical properties, *J. Alloys Compd.* 541 (2012) 177–185. [doi:10.1016/j.jallcom.2012.07.022](https://doi.org/10.1016/j.jallcom.2012.07.022).
- [47] H. Galarraga, R.J. Warren, D.A. Lados, R.R. Dehoff, M.M. Kirka, Fatigue crack growth mechanisms at the microstructure scale in as-fabricated and heat treated Ti-6Al-4V ELI manufactured by electron beam melting (EBM), *Eng. Fract. Mech.* 176 (2017) 263–280. [doi:10.1016/J.ENGFRACMECH.2017.03.024](https://doi.org/10.1016/J.ENGFRACMECH.2017.03.024).
- [48] Y. Zhai, D.A. Lados, E.J. Brown, G.N. Vigilante, Fatigue crack growth behavior

- and microstructural mechanisms in Ti-6Al-4V manufactured by laser engineered net shaping, *Int. J. Fatigue*. 93 (2016) 51–63. doi:10.1016/j.ijfatigue.2016.08.009.
- [49] S.R. Stock, M.A. Langøy, Fatigue-crack growth in Ti-6Al-4V-0.1Ru in air and seawater: Part II. crack path and microstructure, *Metall. Mater. Trans. A*. 32 (2001) 2315–2324. doi:10.1007/s11661-001-0205-8.